

How Transition Metals Enable Electron Transfer through the SEI: Part II. Redox-Cycling Mechanism Model and Experiment

Oliver C. Harris, 61,* Kevin Leung, 2,** and Maureen H. Tang 61,**, Z

¹Drexel University, Philadelphia, Pennsylvania 19104, USA

At high operating voltages, metals like Mn, Ni, and Co dissolve from Li-ion cathodes, deposit at the anode, and interfere with the performance of the solid-electrolyte interphase (SEI) to cause constant Li loss. The mechanism by which these metals disrupt SEI processes at the anode remains poorly understood. Experiments from Part I of this work demonstrate that Mn, Ni, and Co all affect the electronic properties of the SEI much more than the morphology, and that Mn is the most aggressively disruptive of the three metals. In this work we determine how a proposed electrocatalytic mechanism can explain why Mn contamination is uniquely detrimental to SEI passivation. We develop a microkinetic model of the redox cycling mechanism and apply it to experiments from Part I. The results show that the thermodynamic metal reduction potential does not explain why Mn is the most active of the three metals. Instead, kinetic differences between the three metals are more likely to govern their reactivity in the SEI. Our results emphasize the importance of local coordination environment and proximity to the anode within the SEI for controlling electron transfer and resulting capacity fade.

© The Author(s) 2019. Published by ECS. This is an open access article distributed under the terms of the Creative Commons Attribution 4.0 License (CC BY, http://creativecommons.org/licenses/by/4.0/), which permits unrestricted reuse of the work in any medium, provided the original work is properly cited. [DOI: 10.1149/2.0032001JES]

Manuscript submitted May 29, 2019; revised manuscript received July 24, 2019. Published August 26, 2019. This paper is part of the JES Focus Issue on Mathematical Modeling of Electrochemical Systems at Multiple Scales in Honor of Richard Alkire.

Electrode crosstalk in high-voltage Li-ion batteries accelerates capacity fade in these devices, prohibiting commercialization and utilization in electrified vehicles. Crosstalk is the mechanism by which transition metals dissolve from the transition metal oxide positive electrode, transport to the negative electrode, and then deposit in the solid-electrolyte interphase (SEI). $^{1-4}$ Transition metal contamination of the SEI has been widely demonstrated to alter the composition, morphology, and performance of this important interface, resulting in continual Li consumption and electrolyte decomposition. $^{2.5-8}$ Layered NMC (LiNi $_{\rm x}$ Mn $_{\rm y}$ Co $_{\rm z}$ O $_{\rm z}$) is a class of promising cathode active materials for high-voltage Li-ion batteries that suffers from electrode crosstalk. $^{3.7,9-12}$ While the effects of metal dissolution from NMC cathodes on battery lifetime and capacity are well understood, the precise mechanism by which Mn, Ni, and Co individually contribute to SEI failure remains unclear.

The most common explanations are that a) these metals deposit in a metallic state and undermine the electron-blocking nature of the SEI, 4.13 b) incorporation of the metals into the SEI causes cracking which allows constant electrolyte reduction, 5.13,14 or c) that these metals undergo catalytic cycling to receive electrons from the anode and then transfer them to reduce electrolyte or degrade SEI constituents. 5,7,8,15–18 In previous work, we identified the electrocatalytic mechanism as the most likely explanation by finding that Mn contamination of the SEI significantly alters the electronic properties of the SEI, while only mildly affecting the morphological properties. Here we develop a microkinetic model of electrocatalytic metal cycling in the SEI and apply it to our experiments from Part I to investigate the individual role of Mn, Ni, and Co in facilitating through-film charge-transfer.

Summary of key findings in part I.—In Part I of this work,³² we measured the individual effects of Mn, Ni, and Co on SEI formation and through-film charge transfer. SEIs were formed by cycling glassy carbon electrodes to low voltages in commercial LP 30 electrolyte both in the absence and presence of transition metal acetylacetonate salts. In metal-contaminated electrolyte, new reduction peaks were seen on the cyclic voltammograms that were not apparent in metal-free electrolyte, indicating transition metal reduction and incorporation into the forming SEI. The formed SEIs were probed via an in-situ electrochemical characterization method using ferrocenium to probe the de-

gree of passivation. Voltammograms of ferrocenium reduction through metal-free and metal-contaminated SEIs were interpreted via a Butler-Volmer kinetic model to identify each metal's effect on through-film charge-transfer.

One of the key findings in Part I³² is that Mn contamination has a more detrimental effect on SEI passivation than Ni and Co. This agrees with the recent findings of Jung and Solchenbach in which intentionally Mn-contaminated cells showed lower coulombic efficiencies and greater capacity fade than cells with Ni- and Co-contaminated electrolyte, 17 and Mn-contamination showed a more severe effect on gas evolution than Ni contamination. ¹⁸ In agreement with previous work using the more sensitive ICP-OES technique, ¹⁷ Part I demonstrated through energy dispersive X-ray (EDX) that these metals deposited in the SEI in equally dilute concentrations.³² Interestingly, all metals had similar effects on SEI electronic and morphologic properties, though to varying degrees. Contamination by each metal increased through-film kinetics more significantly than through-film transport, hinting that the mechanism of charge-transfer involves facile electron transfer at these metal sites. A physics-based model of the SEI¹⁹ was used to better interpret why Mn is more detrimental to SEI passivation than Ni, and Ni more than Co, and this analysis found that the electron-transfer rate at embedded Mn is greater than that for Ni and Co. Part II of this work develops and applies a microkinetic model of electrocatalytic metal cycling to experimental data from Part I in order to elucidate the difference in electron-transfer rates between Mn, Ni, and Co.

Model Development

The proposed scheme has two elementary steps. M denotes an isolated transition metal ion embedded within the SEI that can be electrochemically reduced.

Reaction 1:
$$M^{2+} + e^{-} \leftrightarrow M^{+}$$

The reduced metal then reacts chemically with the ferrocenium cation:

Reaction 2:
$$FCN^+ + M^+ \leftrightarrow M^{2+} + FCN$$

The net reaction is indistinguishable from the simple Butler-Volmer model of Part I:

Net reaction:
$$FCN^+ + e^- \leftrightarrow FCN$$

In this work, only single-electron reduction of M^{2+} to M^+ is considered, while M(0) is not considered. The aim of this work is to

² Sandia National Laboratory, Albuquerque, New Mexico 87185, USA

^{*}Electrochemical Society Student Member.

^{**}Electrochemical Society Member.

^zE-mail: mhtang@drexel.edu

evaluate the mechanism of SEI decomposition proposed by Joshi and others^{5,6,7,8,15–18} using experimental data collected in Part I,³² thus our modeling applies the single-electron reduction assumption from those proposed mechanisms. Additionally, the existence of M(0) within the SEI has been contested by recent in-situ studies⁶ which find only Mn²⁺. Lastly, if the metal contaminants deposit in the metallic state and form a conductive SEI, the voltammograms collected in Part I³² would be linear throughout the potential range, which is not observed. Thus, our analysis and reaction scheme proceeds assuming a single-electron reduction of M²⁺ to M⁺ and without considering M(0).

In principle, either Reaction 1 or 2 could be the rate-limiting step of the overall reaction scheme. However, ferrocenium reduction is intrinsically a fast, outer-sphere reaction, and the hypothesized M⁺ is a highly unstable intermediate that should decompose rapidly. ¹⁶ Furthermore, simulations with Reaction 2 as the rate-limiting step (not shown) yielded voltammograms with no voltage dependence, inconsistent with experiment. Accordingly, Reaction 2 is assumed to be equilibrated and the electrochemical metal reduction in Reaction 1 is the rate-limiting step in all subsequent analysis. Reaction 2 is a proxy for electrolyte and SEI degradation, as well as SEI growth, on a graphite electrode. The SEI growth reactions are much less reversible than ferrocenium reduction. However, the use of the reversible couple experimentally isolates kinetic effects of Reaction 1, the metal reduction step.

Following, the rate expressions for these two reactions are²⁰

$$r_{1} = k_{c}C_{M^{2+}}exp\frac{-\alpha_{c}nF}{RT}V - k_{a}C_{M^{+}}exp\frac{\alpha_{a}nF}{RT}V$$

$$r_{2} = k_{f}C_{FCN}+C_{M^{+}} - k_{b}C_{FCN}C_{M^{2+}} = 0$$
[1]

where k_a , k_c are the anodic and cathodic rate constants for Reaction 1, α_a , α_c are the anodic and cathodic transfer coefficients for Reaction 1, and k_f , k_b are the forward and backward rate constants for Reaction 2. n, F, R, and T are the number of electrons, Faraday's constant, gas constant, and temperature, respectively. The equilibrium constant $K_{eq,2}$ is

$$K_{eq,2} = \frac{k_f}{k_b} = \frac{C_{M^{2+}}C_{FCN}}{C_{M+}C_{FCN+}}$$
 [2]

 $K_{eq,2}$ can be related to the reaction potentials by.

$$K_{eq,2} = exp\left(\frac{nF}{RT}\left(U_{FCN^{+}/FCN}^{\Theta} - U_{M^{2+}/M^{+}}^{\Theta}\right)\right) = exp\left(fU_{FCN-M}^{\Theta}\right)$$

where f = F/RT, U_{FCN-M}^{Θ} is the voltage difference between the standard reduction potentials of ferrocenium and the transition metal, and n = 1 for this single electron reaction. We define ξ as the fraction of reduced metal and then solve for ξ as a function of ferrocene and ferrocenium surface concentrations:

$$\xi = \frac{C_{M^{+}}}{C_{M^{+}} + C_{M^{2+}}} = \frac{C_{M^{+}}}{C_{M,tot}}$$

$$\xi = (1 - \xi) \frac{C_{FCN}}{C_{FCN^{+}}} K_{eq,2} = \frac{C_{FCN}}{C_{FCN} + C_{FCN} + exp\left(fU_{FCN-M}^{\theta}\right)}$$
[4]

Assuming that n=1 for Reaction 1, $\alpha_c=1-\alpha_a$. Inserting ξ into the rate expression:

$$\frac{r_1}{C_{M,tot}} = k_c (1 - \xi) \exp\left(-(1 - \alpha_a) fV\right) - k_a \xi \exp\left(\alpha_a fV\right)$$
 [5]

Current is expressed in a pseudo-Butler-Volmer form by introducing the surface overpotential, η_s , defined by $V = U^{\Theta}_{M^{2+}/M^+} + \eta_s$. When Reaction 1 is at equilibrium, $V = U^{\Theta}_{M^{2+}/M^+}$ and $i_n = \mathbf{r}_1 = 0$. This yields the following relationship between ξ and $U^{\Theta}_{M^{2+}/M^+}$:

$$U_{M^{2+}/M^{+}}^{\Theta} = \frac{1}{f} ln \left(\frac{k_{c} (1 - \xi)}{k_{a} \xi} \right)$$
 [6]

Inserting this into the rate expression,

$$\frac{i_n}{FAC_{M,tot}} = k_a \xi exp \left\{ \alpha_a f \left[\eta_s + \frac{1}{f} ln \left(\frac{k_c (1 - \xi)}{k_a \xi} \right) \right] \right\} - k_c (1 - \xi) \\
\times exp \left\{ - (1 - \alpha_a) f \left[\eta_s + \frac{1}{f} ln \left(\frac{k_c (1 - \xi)}{k_b \xi} \right) \right] \right\} \quad [7]$$

The exchange current density, i_0 , and effective rate constant, k_{eff}

$$i_0 = F k_{eff} C_{M^+}^{1-\alpha_a} C_{M^{2+}}^{\alpha_a}$$
 [8]

$$k_{eff} = k_a^{1 - \alpha_a} k_c^{\alpha_a} \tag{9}$$

$$i_n = i_0 \{ exp [\alpha_a f \eta_s] - exp [-(1 - \alpha_a) f \eta_s] \}$$
 [10]

To fit the raw experimental i-V data to this reaction mechanism, at each value of i_n the surface concentrations of ferrocene and ferrocenium are calculated by

$$C_{FCN^+} = C_{FCN^{+,\infty}} \left(1 - \frac{i_n}{i_{lim,f}} \right)$$

$$C_{FCN} = C^{\infty} - C_{FCN^+}$$
 [11]

where $C_{FCN^{+,\infty}}$ is the bulk concentration of ferrocenium and C^{∞} is the total bulk concentration of ferrocene and ferrocenium. The reversible potential is calculated according to the Nernst equation by

$$E_{rev} = E^0 + \frac{1}{f} ln \left(\frac{C_{FCN^+}}{C_{FCN}} \right)$$
 [12]

And the fraction of reduced metal is calculated according to Eq. 4:

$$\xi = (1 - \xi) \frac{C_{FCN}}{C_{FCN^{+}}} K_{eq,2} = \frac{C_{FCN}}{C_{FCN} + C_{FCN} + exp(fU_{FCN-M}^{\theta})}$$

The fitting parameters are the anodic transfer coefficient, α_a , the effective heterogenous rate constant, k_{eff} , and the through-film limiting current, $i_{lim.f}$. Because the standard reduction potential for the transition metal, U_M^Θ , is not well-known from the literature, it can also be treated as a fitting parameter. With these parameters, the exchange current density, i_0 , is calculated according to Eq. 8 and the Butler-Volmer potential, E_{BV} , is found by solving the following

$$\frac{i_n}{i_0} = exp\left[\alpha_a f E_{BV}\right] - exp\left[-\left(1 - \alpha_a\right) f E_{BV}\right]$$
 [13]

The ohmic contribution to the total potential is calculated according to Ohm's law by

$$E_{\Omega} = i_n R_{\Omega} \tag{14}$$

The total potential at that value of i_n is the sum of the various potential contributions

$$E_{tot} = E_{rev} + E_{BV} + E_{\Omega}$$
 [15]

The goodness of fit for simulated voltammograms is evaluated by comparing plots of i_n vs. E_{tot} and experimentally collected i_n vs. V.

Model validation.—Figure 1 shows the effect of each fitting parameter on a simulated voltammogram for a Mn-contaminated SEI, with a good fit represented by the series with maroon circles in all four plots. According to Figure 1a, increasing the anodic transfer coefficient, α_a , for the metal reduction reaction, without changing the other parameters, results in a steeper Tafel region while decreasing the coefficient flattens the current response. In Figure 1b the effect of the metal reduction potential on the simulated voltammogram is shown, where a higher reduction potential of the reaction increases the current response but does not have a drastic effect on the flatness of the curve. Figure 1c shows the effect of ohmic resistivity, R_{ohm} , on the shape of the voltammogram, where a greater resistivity pushes the "knee" of the voltammogram to lower potentials and distorts

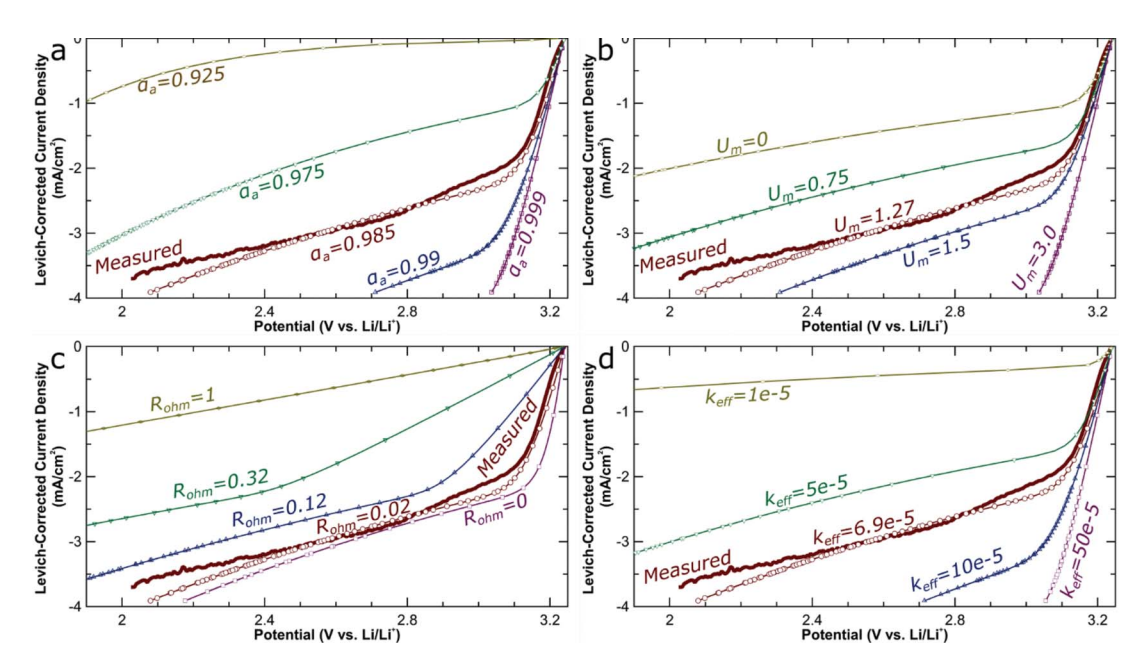


Figure 1. Comparison of fitting parameter variation to Levich-corrected experimental data for a Mn-contaminated SEI. (a) Anodic transfer coefficient, α_a ; (b) Transition metal reduction potential, U_m , vs. Li/Li⁺; (c) resistivity, R_{ohm} , kΩ-cm;² (d) Effective kinetic rate constant, k_{eff} , cm/s. Open maroon circles represent a best fit and the maroon lines are the Levich-corrected experimental data.

the Tafel region. Varying α_a or U_M in Figure 1a and Figure 1b does not greatly affect the potential of this knee, but does affect the current at the knee potential. Finally, Figure 1d shows simulated voltammograms for a range of the effective rate constant, k_{eff} , and as expected, larger rate constants result in more current passing through the SEI. The effect of k_{eff} and U_M is identical, consistent with the Tafel equation for irreversible kinetics. With this unsurprising exception, the combined results of Figure 1 show that the fitting parameters of α_a , $R_{\rm ohm}$, and k_{eff} have unique effects on the simulated current response and validate our model.

According to Figure 1, the anodic transfer coefficient, α_a , is the parameter with the greatest effect on the shape of the curve. This is reinforced in Figure 2, which shows how adequate fits of the experimental data are only achievable within a certain range of this parameter. In Figure 1a, the other fitting parameters are held constant, whereas in Figure 2a the effective rate constant, k_{eff} , and ohmic resistivity, R_{ohm} , are varied to achieve the best fit possible. It is clear that for this single experimental trial of a Mn-contaminated SEI, an anodic transfer coefficient of between 0.98 and 0.99 is needed to achieve a reasonable model fit, with 0.985 providing the best fit. Figure 2b shows that an anodic transfer coefficient of 0.90 cannot provide a reasonable fit for this experimental trial, indicating that agreement between the microkinetic model and experimental data is constrained to a relatively limited parameter space.

$$E_{tot} = E_{BV} + E_{\Omega} + E^{0} + U_{FCN-M}^{\Theta} + \frac{1}{f} ln \left(\frac{1-\xi}{\xi} \right)$$
 [16]

Equation 16 shows how the mediator reaction redox potential is composed of contributions from Butler-Volmer kinetics, ohmic resistance, mediator standard reduction potential, metal standard reduction potential, and reduced metal concentration. Equation 16 combines Equations 4, 12, and 15 and directly compares experimentalto simulated voltammograms. The last term of Equation 16 represents the entropic contribution to the metal reduction potential. When \S , the fraction of reduced metal, approaches zero the entropic contribution to the equilibrium redox potential is very high, and metal reduction occurs at potentials above the standard reduction potential, U_M^{Θ} . This demonstrates why, for example, in Figure 1b and Figure 2, the potential range of the cyclic voltammograms is several hundred millivolts

greater than the metal reduction potentials for Mn, U_{Mn}^{Θ} , yet our reaction scheme shows that Mn is reduced at these high potentials.

Computational details.—Density Functional Theory (DFT) calculations apply the Gaussian 09 suite of programs,²¹ the PBE0 functional,²² the LANL2DZ ECP potentials,²³ and the SMD

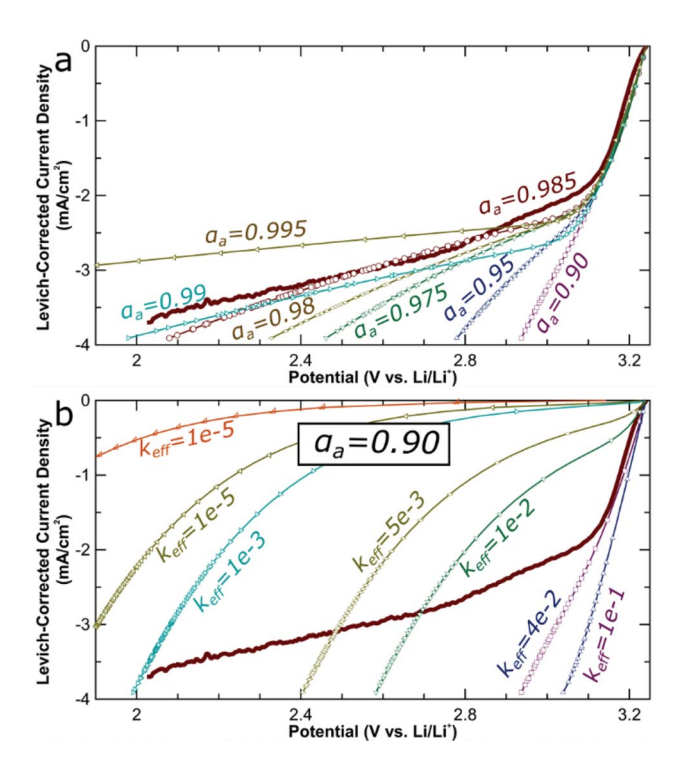


Figure 2. Strict tolerance of anodic transfer coefficient values for adequate model fitting. (a) Poor fitting of model to Levich-corrected experimental data for certain values of anodic transfer coefficient, α_a ;(b) Simulated voltammograms do not match experimental data when anodic transfer coefficient, α_a , is set to 0.90. Open maroon circles represent a best fit and the maroon lines are the Levich-corrected experimental data.

solvation method. ²⁴ Each simulation cell contains six EC molecules plus one transition metal cation (triplet Co+, doublet Co²⁺, singlet Co³⁺, doublet Ni+, triplet Ni²⁺, doublet Ni³⁺, quintet Mn+, sextet Mn²⁺, and quintet Mn³⁺). A static dielectric constant (ϵ_o) of 40, relevant to the region outside the explicit solvent molecules, reflects the dielectric response from a mixture of EC and DMC. The absolute solvation free energies and the absolute redox potentials depend on the choice of ϵ_o . However, changing ϵ_o would to a first approximation only affect the electrostatic contribution to the redox potential, which is similar for all three transition metal ions undergoing the same change in charge states. The d-orbital crystal field splitting portion of the redox potential, distinct for Co, Mn, and Ni, should be unaffected by the choice of ϵ_o . Therefore the relative redox potentials for these cations should be insensitive to ϵ_o .

Results and Discussion

Direct comparison of measured current for metal-contaminated SEI of Mn, Ni, and Co.—The kinetic expressions of Equations 8, 9, and 10 represent only the current, i_{metal} , that occurs at catalytic metal sites, and do not include the current due to pinholes in the metal-free SEI, i_{PH} . These two pathways can be deconvoluted considering the reaction scheme in Figure 3 and the control (metal-free) data in Figure 3 in Part I.

As seen in Figure 3 in Part I, there are three voltammograms of ferrocenium reduction through metal-free SEIs (gray curves) for each transition metal, because three different glassy carbon working electrodes were used to ensure each electrode was only exposed to one transition metal. The average of the three metal-free voltammograms are corrected for the Levich resistance to obtain i_{PH} , the upper branch in Figure 3b, by:

$$i_{PH} = \frac{i_{lim,\infty}i_{metal-free}}{i_{lim,\infty}-i_{metal-free}}$$
[17]

where $i_{lim,\infty}$ is the limiting current for ferrocenium reduction on a pristine electrode (i.e. no SEI) and is given by the Levich equation. The raw experimental data for each metal-contaminated trial, $i_{t\alpha}$, is similarly corrected for the Levich resistance, according to

$$i_{PH} + i_{metal} = \frac{i_{lim,\infty}i_{tot}}{i_{lim,\infty} - i_{tot}}$$
[18]

and $i_{PH}+i_{metal}$ is all current attributed to reactions in the SEI. Subtracting i_{PH} from i_{tot} after the Levich correction yields the current that can be attributed to metal-mediated ferrocenium reduction, i_{metal} . Figure 3c shows the reaction scheme for this metal-mediated ferrocenium reduction. An example of this correction process for a single trial of each metal is shown in Figure 4. Comparing Figure 4a, Figure 4b, and Figure 4c for Mn, Ni, and Co, respectively, the contribution of i_{PH} to the total current through a metal-contaminated SEI is greatest for Co than for Ni and Mn. Figure 4d shows representative i_{metal} curves for the three metals. Mn displays the fastest kinetics (steepest slope at low overpotential) and transport (largest current at high overpotential). Ni exhibits faster kinetics than Co though with similar through-film transport. Additionally, simulated voltammograms for metal-mediated ferrocenium reduction according to the above model (hollow circles) are overlaid on the corrected experimental data in Figure 4d. Thus, the metal-mediated ferrocenium reduction model can be used to analyze differences in i_{metal} between Mn, Ni, and Co.

Investigating the roles of thermodynamics and kinetics in metal-mediated reduction.—Our data shows clearly that Mn contamination of the SEI allows more through-film electron transfer than Ni, and Ni allows more than Co. Butler-Volmer analysis shows that the differences between metal kinetics can be explained by differences in concentration or activity of metal sites. The transition metal-mediated ferrocenium reduction model introduces a new possible explanation for these differences: the thermodynamic potential of the M²⁺/M⁺ redox couple. If the concentration and activity of the metals are all equal,

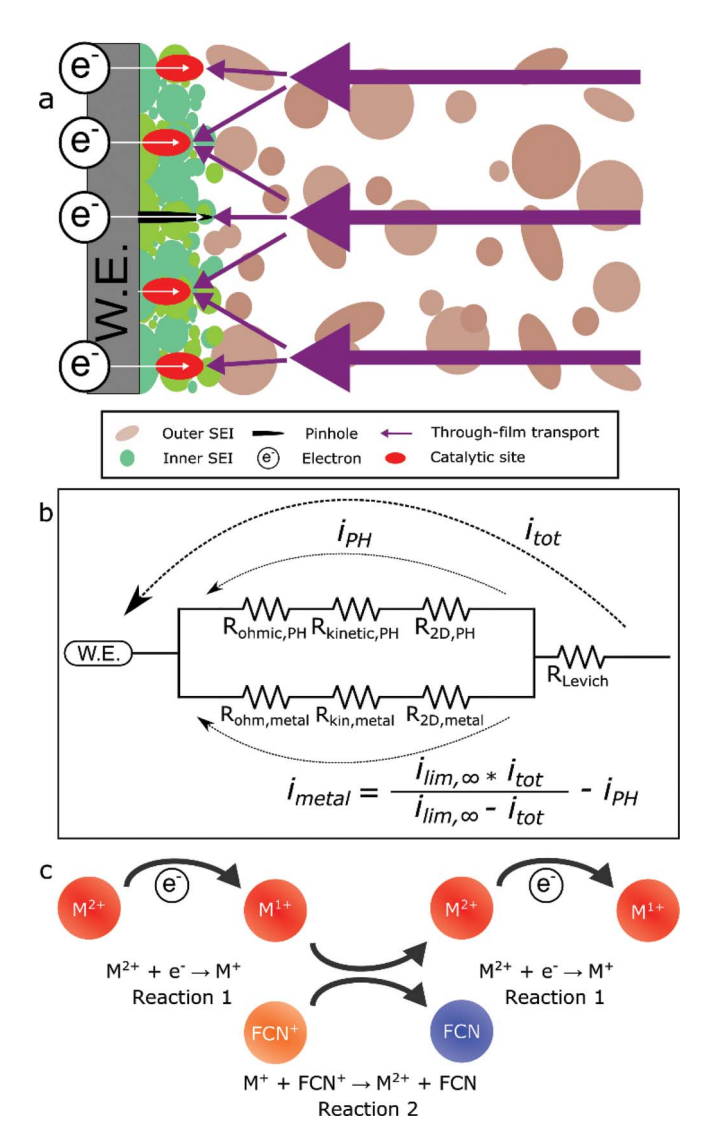


Figure 3. Possible mechanism of SEI interference by metals and equivalent circuit of SEI transport and kinetics. (a) Schematic of charge transfer through a metal-contaminated SEI with a metal-free pinhole and metallic catalytic sites for metal-mediated SEI degradation; (b) Equivalent circuit of metal-contaminated SEI with a metal-free pinhole and metallic catalytic sites; (c) Reaction scheme of transition metal induced electrocatalytic cycle for ferrocenium reduction.

then the differences in standard reduction potential could offer insight into why Mn degrades the SEI to a greater extent than Ni and Co.

Comparing reaction kinetics and through-film transport between the different transition metals requires the metal reduction potential, U_M^0 for Mn, Ni, and Co. There are very few actual reports of the reduction potentials for transition metal cations in organic carbonate electrolytes. Values in Komaba et al. were not directly measured but rather taken from the aqueous reduction potentials. ²⁶ Jung et al. recently reported reduction potentials for Mn²⁺, Ni²⁺, and Co²⁺ in commercial grade LP57 electrolyte (1M LiPF₆ in EC:EMC 3:7 w:w) of $U_{Mn}^0 = 1.27$, $U_{Ni}^0 = 2.22$, and $U_{Co}^0 = 2.52$ V vs. Li/Li⁺¹⁷. These measured reduction potentials are for M²⁺ to M⁰, and not for the hypothesized single electron reduction reaction that has been proposed and is interrogated by our model. To determine if the same trend of $U_{Co}^0 > U_{Ni}^0 > U_{Mn}^0$ applies to a single-electron reduction, the energetics of solvated M³⁺, M²⁺, and M⁺ were calculated using DFT.

Computational results are shown in Table I. The metals were modeled as isolated cations surrounded by six EC molecules and a dielectric continuum. In other words, liquid EC was used as a proxy for

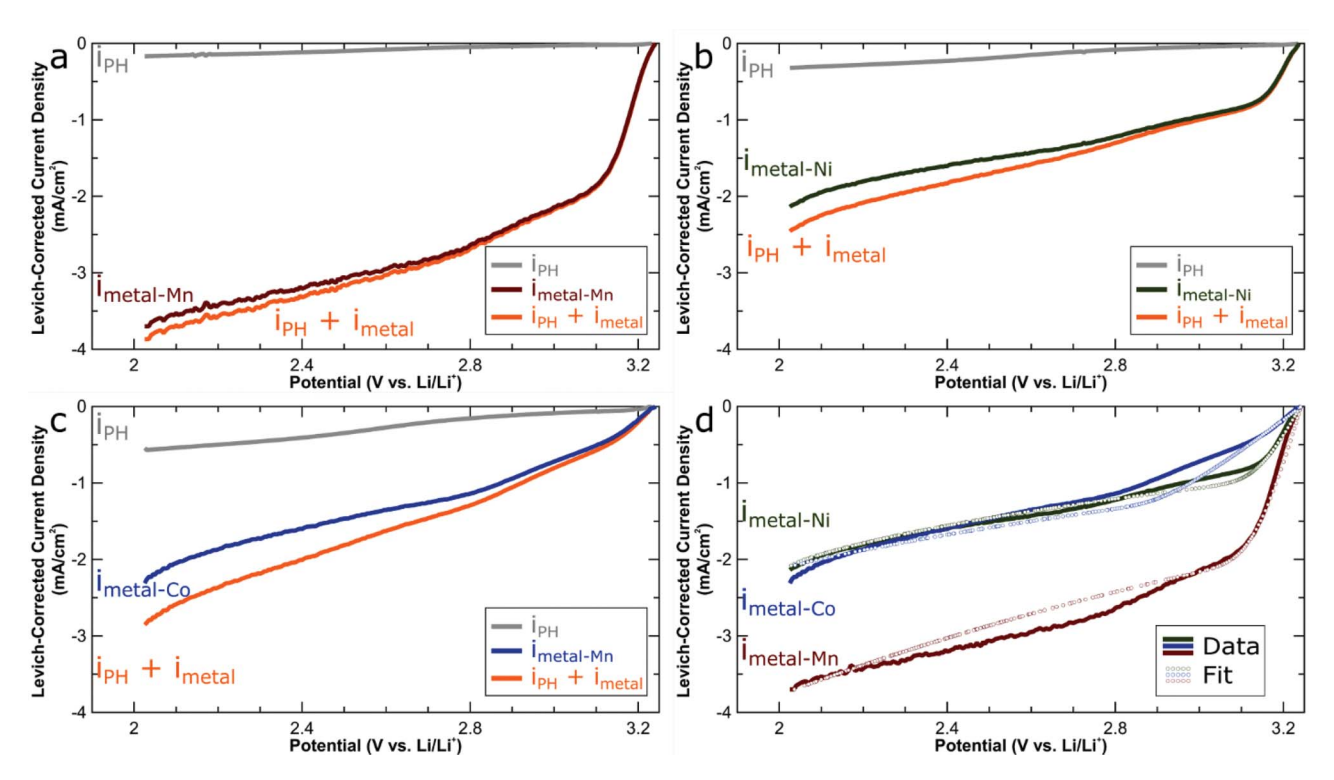


Figure 4. Correcting total current through metal-contaminated SEI for pinhole current to apply metal-mediated ferrocenium reduction scheme. (a) Corrected currents in Mn-mediated ferrocenium reduction model; (b) Corrected currents in Ni-mediated ferrocenium reduction model; (c) Corrected currents in Co-mediated ferrocenium reduction model; (d) Comparison of metal-catalyzed contributions to total current for Mn, Ni, and Co with model fits overlaid as empty circles.

organic components of the SEI. In Figure 5, structures of EC-solvated metal-complexes are shown for Mn (5a, 5b) and Co (5c, 5d). The M⁺ structures (5a, 5c) are formed by adding an excess electron into the M²⁺ solvation complexes (5b, 5d). Most interestingly, the ECsolvated "Mn+" complex is fundamentally different from Co+ and Ni⁺ (not shown). Adding an excess electron to Mn²⁺ solvated by EC leads to that electron being spontaneously injected into one of the 6 EC molecules, which adopts a characteristic bent structure because the carbonyl carbon is now in a sp^3 hybridization (Figure 5a). In contrast, Co²⁺ and Ni²⁺ are electrochemically reduced to Co⁺ and Ni⁺, respectively (Figure 5c). The instability of Mn⁺ compared to Ni⁺ or Co⁺ results in a lower reduction potential. As a result, the calculations predict that, for both $M^{3+} \rightarrow M^{2+}$ and $M^{2+} \rightarrow M^{+}$, Mn is less noble than either Ni or Co, although the predicted nobility of Ni relative to Co varies with the reaction. In Part I of this work, we determined the bandgap of M²⁺- and M⁺-doped LiF. Comparing the cohesive energy gained after inserting a Li+ and an electron and subtracting the cohesive energy of Li metal per atom, we found equilibrium voltages associated with inserting the e^{-}/Li^{+} pair of -2.19, 1.37, and 2.66 V vs. Li⁺/Li(s) for Mn, Ni, and Co, respectively. This calculation again showed the same trend between metals. Thus, it is likely that the trend of $U_{Co}^{\theta} > U_{Ni}^{\theta} >> U_{Mn}^{\theta}$ applies to the single-electron reduction as well as the experimentally measured two-electron potentials reported by Jung et al. 17

In the microkinetic model, the anodic transfer coefficient, α_a , was set to 0.985 for all three metals to isolate the effect of the redox poten-

Table I. Predicted thermodynamic reduction potentials of metal cations.

Reaction	Solvation environment	M = Mn	M = Ni	M = Co
$M^{2+} \rightarrow M^+$	Liquid EC	0.90 V	1.85 V	1.46 V
$M^{3+} \rightarrow M^{2+}$	Liquid EC	5.93 V	6.46 V	7.19 V
$M^{2+} \rightarrow M^{+}$	Crystalline LiF	-2.19 V	1.37 V	2.66 V

tial U_M , and the kinetic rate constant k_{eff} . This high value of α_a indicates that the structure of the activated complex in the metal reduction reaction is very similar to that of the oxidized M^{2+} species. Consequently, the anodic reaction is strongly dependent on applied potential, whereas the cathodic reaction is very weakly dependent. The limiting currents of 2D-diffusion to metal sites, $i_{lim,M}$, were interpreted from

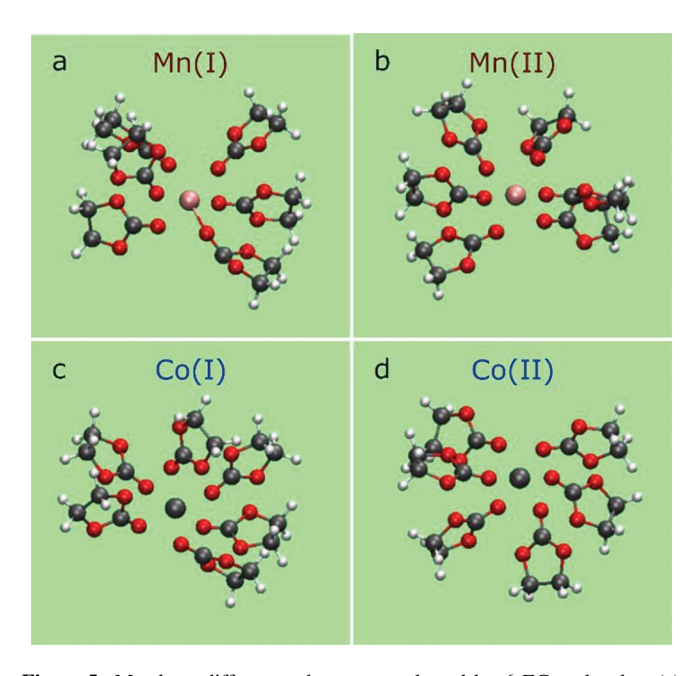


Figure 5. Metals at different redox states solvated by 6 EC molecules. (a) Mn^+ with a bent-EC molecule; (b) Mn^{2+} ; (c) Co^+ does not eject the excess electron and is metastable; (d) Co^{2+} . Ni^+ and Ni^+ structures are not shown, but are similar to Co^+ and Co^{2+} , respectively.

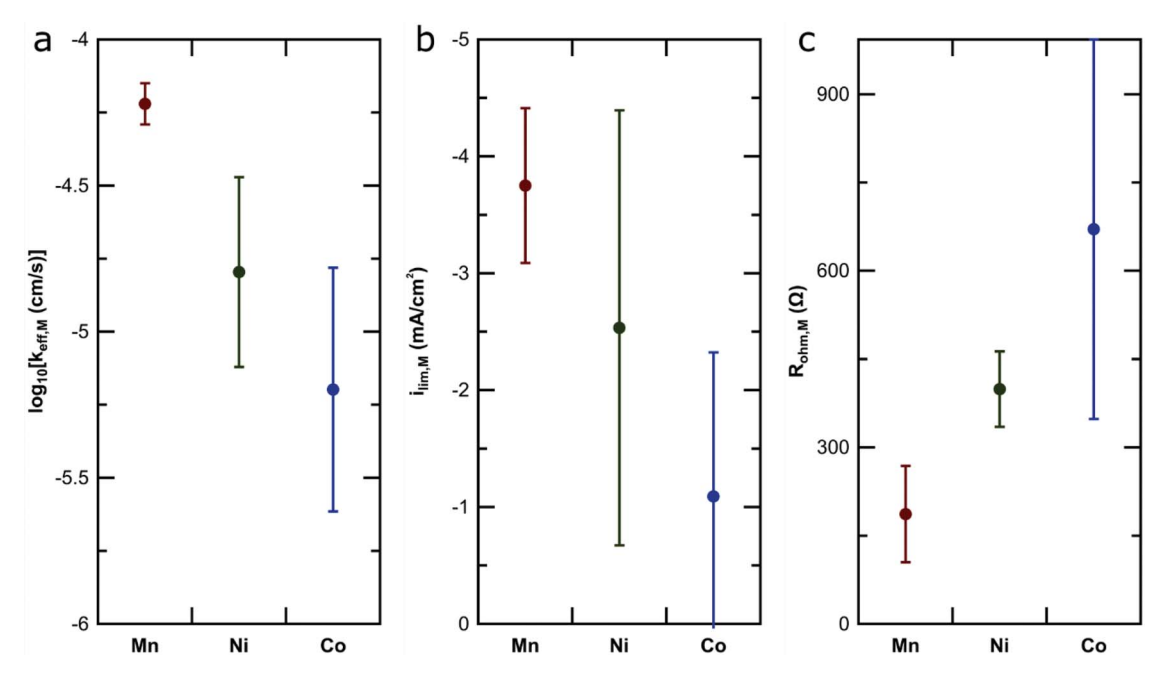


Figure 6. Fitting parameters for transition-metal mediated ferrocenium reduction in contaminated SEIs on glassy carbon electrodes. Circles represent mean of model fits on three experimental trials, error bars represent one standard deviation. (a) Log effective kinetic rate constant at metal site, $log_{10}(k_{eff,M})$; (b) Through-film limiting currents, $i_{lim,M}$; (c) resistance to metal site, $R_{ohm,M}$. Error bars represent one standard deviation from the mean for three experimental trials.

plots of $ln(i_{metal})$ vs. V for each experimental trial, and the standard reduction potentials, U_M^{θ} , were set according to the findings of Jung's recent work.¹⁷ The effective heterogenous rate constants of metal reduction, $k_{eff,M}$, and the ohmic resistances of the films, $R_{ohm,M}$, were determined for each experimental trial under the above conditions. The mean values of all three trials are shown in Figure 6 with error bars representing one standard deviation. Once again, clear trends emerge from Mn to Ni to Co: kinetics are fastest with Mn and slowest with Co, transport to metal sites are fastest with Mn and slowest with Co, and contaminated films are least resistive with Mn and most resistive with Co. In Figure 6a, the mean effective heterogenous rate constant for the reduction of the three metals are shown, and Mn reduction is approximately five times faster than Ni reduction, and greater than 1 order of magnitude faster than Co reduction. Additionally, Figure 6b shows a similar trend to Figure 6b in Part I indicating again that diffusion to the metal site is faster for Mn than Ni and Co, which may be attributed to either differences in metal site size or density within the SEI. Figure 6c demonstrates a lower ohmic resistance in electron transfer to Mn sites than Ni sites and Co sites. This may indicate that the SEI around Mn sites is less insulating, or less mineralized, than the SEI around Ni and Co sites, thereby allowing electron transfer from the negative electrode to the metal site with lower resistance. Another explanation could be a shorter distance between Mn and the negative electrode than for Ni or Co.

The model fits in Figure 6 assume that $U_{Mn}^{\theta} < U_{Ni}^{\theta} < U_{Co}^{\theta}$, in accordance with findings from Solchenbach and Jung $^{1/18}$ as well as DFT results in Table I. However, it is also instructive to independently investigate the role of metal reduction potentials by setting the effective rate constants equal (i.e., $k_{eff,Mn} = k_{eff,Ni} = k_{eff,Co} = 10^{-3} \frac{cm}{s}$) and the role of reaction kinetics by setting the standard reduction potentials equal (i.e., $U_{Mn}^{\theta} = U_{Ni}^{\theta} = U_{Co}^{\theta} = 2$ V vs. Li/Li⁺).

Isolating the effects of metal reduction potential and kinetics on sei degradation.—By setting the kinetics of metal reduction to be equally fast for all metals, reasonable model fits are found by varying the standard reduction potentials for these metals. Figure 7a demonstrates that if thermodynamics of the metal reduction reaction is isolated as the main driving force for reaction, then Mn must be the most noble of the three metals and Co the least. This is contrary to both aque-

ous and non-aqueous experimental measurements of $\mathrm{Mn^{2+}}$, $\mathrm{Ni^{2+}}$, and $\mathrm{Co^{2+}}$ reduction 17,26 and DFT calculations, which found Mn to be the *least noble* of the three metals. One possibility is that the metal reduction potentials within the SEI are governed at the molecular level by local phenomena such as coordination environment, rather than the bulk phenomena that typically determine metal reduction. This effect could potentially result in a counter-intuitive trend of $U_{Mn}^{\theta} > U_{Ni}^{\theta} > U_{Co}^{\theta}$. Another possibility is that thermodynamics do not adequately account for the different behavior of these metals embedded within the SEI because the kinetics of the reaction dominate the system.

The effect of kinetics is quantified by setting the reduction potentials equal for all metals and then varying the kinetic rate constant to fit the experimental data. Figure 7b shows the results with these assumptions. Comparison to Figure 6a demonstrates that assuming equal reduction potentials decreases the discrepancy in kinetic rate constants. When the reduction potentials are taken from literature, ¹⁷ the rate constant for Mn reduction, $k_{eff,Mn}$, is over one order of magnitude greater than for Co reduction, $k_{eff,Co}$, but when the potentials are assumed to be equal, $k_{eff,Mn}$ is less than an order of magnitude faster than $k_{eff,Co}$. Thus, if the metal reduction potential is an important descriptor of electron-transfer through the SEI, then it cannot also simultaneously explain why Mn is more detrimental to SEI performance than Ni and Co.

Possible molecular origins of thermodynamic and kinetic differences between metal reduction reactions.—If the thermodynamic reduction potentials truly follow $U_{Mn}^{\theta} > U_{Ni}^{\theta} > U_{Co}^{\theta}$, the coordination environment of the metals embedded within the SEI could explain the counter-intuitive trend. Jarry et al. reported that Mn and Ni were always in the 2+ oxidation within the SEI and were surrounded by beta-diketonate ligands, as well as carbonate and oxalate anions, 27 while Solchenbach et al. reasoned that a Mn-contaminated SEI might be more stable and degrade less if the Mn sites were surrounded by compounds that cannot be easily reduced, such as LiF or Li₂CO₃. 18 Jarry et al. also found that the within the SEI, Ni²⁺ was mostly in the form of NiCO₃, whereas Mn²⁺ was mostly in the form of Mn(AcAc)₂. 27 Table I shows that the trend of $U_{Mn}^{\theta} < U_{Ni}^{\theta} < U_{Co}^{\theta}$ holds across reactions and solvation environments, but predicts that values differ between organic and inorganic solvent by up to 3 V. Combining these findings leads to

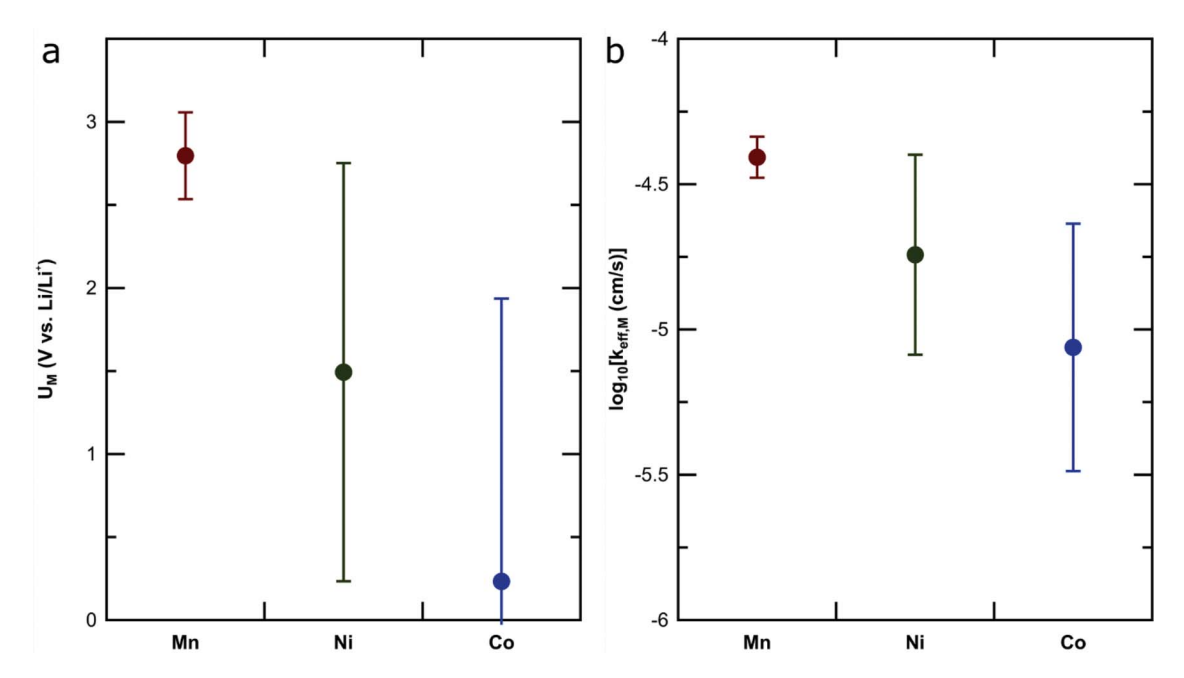


Figure 7. Isolated effects of thermodynamics and kinetics on metal-mediated ferrocenium reduction; (a) Model-predicted values of standard reduction potential, U_M , for each metal when kinetics assumed equal; (b) Model-predicted values of effective rate constant, $k_{eff,M}$, for each metal when reduction potentials assumed equal. Error bars represent one standard deviation from the mean for three experimental trials.

the conclusion that Mn may be more detrimental to SEI performance, and exhibits faster reduction kinetics, because it remains coordinated to polarizable organic ligands, whereas Ni, and possibly Co, are more likely bonded to less polarizable species like fluorides, carbonates and oxalates. The coordination chemistry of metal complexes has an enormous effect on the reduction potential of those metals as well as the electron transfer kinetics of these complexes. Thus, the reduction potentials that affect electron transfer through the SEI may be determined by Mn in a primarily organic environment vs Ni and Co in an inorganic environment.

If the metal reduction potentials are assumed to follow the trend of $U_{Mn}^{\theta} < U_{Ni}^{\theta} < U_{Co}^{\theta}$, Mn must have reduction kinetics that are an order of magnitude faster than Co. The origin of these kinetic variations could be a difference in the distance between the electrode and the metal catalytic sites. The probability of electron tunneling, T, decreases exponentially with distance d via

$$T \propto \exp\left(-\frac{4\pi d}{h}\sqrt{2m\Delta E_t}\right)$$

where m is the mass of an electron, h is Planck's constant, and ΔE_t is the barrier height. Lin et al. calculated ΔE_t for LiF, Li₂CO₃, and Li₃PO₄ ranging from 1.8–6.3 eV, depending on species and computational method.³¹ For these values of barrier height, a difference in d of 2–4 Å would be sufficient to decrease the tunneling probability by a factor of 200. Thus, a slightly smaller distance between the carbon electrode and Mn²⁺ could explain all of the observed kinetic differences. Shkrob suggested that Mn is located at the interface between the organic and inorganic SEI layers.⁸ If Co and Ni are instead embedded within the organic SEI only, such a difference could explain the decreased reactivity of these metals.

Conclusions

In Part I, we showed that the through-film kinetics of electron transfer are much faster through a Mn-contaminated SEI than through an SEI contaminated by Ni or Co. Part II interprets these experimental results through a rigorous microkinetic model of metal redox cycling as the mechanism of electron transfer through the SEI. The model describes experimental data well if the anodic transfer coefficient α_a is

constrained to 0.98-0.99, suggesting that the structure of the activated complex in the metal reduction reaction mostly resembles the oxidized metal species, M²⁺. Using redox potentials for Mn²⁺, Ni²⁺, and Co²⁺ reduction from recent literature, we show that the starkest difference between the three metals is the kinetics of the metal reduction step (Reaction 1). These kinetic differences must dominate the thermodynamic effects of redox potential, which predict that Co should be the most active metal and Mn the least. For thermodynamic redox potentials to explain experimental trends, the changes in the local coordination environment of Mn2+, Ni2+, and Co2+ must be so different that the thermodynamic trends on the bulk metals are reversed. DFT predicts that such large differences are possible if Mn is coordinated to organic ligands while Ni and Co are surrounded by inorganic components. Alternatively, according to previous DFT calculations of electron tunneling barrier height, a difference of 0.2 - 0.4 nm in the distance between the electrode and the isolated transition metal cation would be sufficient to rationalize the observed kinetics. Both the thermodynamic and kinetic explanations for the trends between metal reactivity point to the coordination environment within the SEI as a dominant factor. Mitigating the detrimental effects of metals, especially Mn, on capacity fade in advanced batteries therefore requires better understanding of the local interactions surrounding Mn and their impact on electron transfer.

Acknowledgments

This work was supported by NSF-1751553. KL was supported by Nanostructures for Electrical Energy Storage (NEES), an Energy Frontier Research Center funded by the U.S. Department of Energy, Office of Science, Office of Basic Energy Sciences under Award Number DESC0001160. Sandia National Laboratories is a multi-mission laboratory managed and operated by National Technology and Engineering Solutions of Sandia, LLC, a wholly owned subsidiary of Honeywell International, Inc., for the U.S. Department of Energy's National Nuclear Security Administration under contract DE-NA0003525. This paper describes objective technical results and analysis. Any subjective views or opinions that might be expressed in the paper do not necessarily represent the views of the U.S. Department of Energy or the United States Government.

Appendix

Table A-I. List of Symbols and Meanings.

α_a	Anodic charge transfer coefficient
α_c	Cathodic charge transfer coefficient
η_s	Surface overpotential, $V = U_{M^{2+}/M^+ + \eta_s}^{\Theta}$
ξ	Fraction of reduced metal
C_{FCN}	Surface concentration of ferrocene
C_{FCN^+}	Surface concentration of ferrocenium
$C_{FCN,\infty}$	Bulk concentration of ferrocene in solution
	Bulk concentration of ferrocenium in solution
$C_{FCN^+,\infty} \atop C^{\infty}$	Total bulk concentration of ferrocene and ferrocenium in solution
C_{M^+}	Concentration of partially reduced transition metal
$C_{M^{2+}}$	Concentration of transition metal
	Total concentration of transition metal
$E_{M,tot}^{O}$	Equilibrium potential
E_{Ω}	Ohmic contribution to total potential
E_{BV}	Butler-Volmer potential
E_{rev}	Reversible potential
E_{tot}	Total potential
F	Faraday's constant
f	f = F/RT, lumped Faraday's constant
i_0	Exchange current density
$i_{lim,f}$	Through-film limiting current
$i_{lim,M}$	Limiting current for 2D-diffusion to metal sites
$i_{lim,\infty}$	Limiting current for on a pristine electrode
i_{metal}	Current attributed to metal catalytic sites
$i_{metal-free}$	Total current through metal-free SEI
i_{PH}	Current attributed to pinholes
i_{tot}	Total current through metal-contaminated SEI
k_a	Anodic rate constant for Reaction 1
k_b	Backward rate constant for Reaction 2
k_c	Cathodic rate constant for Reaction 1
k_{eff}	Effective heterogeneous rate constant
$k_{eff,M}$	Model predicted effective heterogeneous rate constant at metal site
$K_{EQ,2}$	Equilibrium constant for Reaction 2
k_f	Forward rate constant for Reaction 2
n	Number of electrons transferred in redox reaction
R	Gas constant
$R_{\omega} = R_{ohm}$	Ohmic resistance
$R_{ohm,M}$	Ohmic resistance at metal site
T	Temperature
$U_{FCN^+/FCN}^{\Theta}$	Standard reduction potential of ferrocenium
U_{FCN-M}^{Θ}	Potential difference between $U^\Theta_{FCN^+/FCN}$ and $U^\Theta_{M^{2+}/M^+}$

Table A-I. Continued

 U_M Model predicted standard reduction potential of transition U_{M^{2+}/M^+}^{Θ} Standard reduction potential of transition metal

ORCID

Oliver C. Harris https://orcid.org/0000-0002-5484-5688 Maureen H. Tang https://orcid.org/0000-0003-0037-4814

References

- 1. W. Choi and A. Manthiram, J. Electrochem. Soc., 153, A1760 (2006).
- 2. D. P. Abraham, T. Spila, M. M. Furczon, and E. Sammann, Electrochem. Solid-State Lett., 11, A226 (2008).
- 3. H. Zheng, Q. Sun, G. Liu, X. Song, and V. S. Battaglia, J. Power Sources, 207, 134
- 4. S. R. Gowda et al., Phys. Chem. Chem. Phys., 16, 6898 (2014).
- 5. T. Joshi, K. Eom, G. Yushin, and T. F. Fuller, J. Electrochem. Soc., 161, A1915 (2014).
- 6. J. Wandt et al., J. Mater. Chem. A, 4, 18300 (2016).
- 7. J. A. Gilbert, I. A. Shkrob, and D. P. Abraham, J. Electrochem. Soc., 164, A389 (2017).
- 8. I. a. Shkrob et al., J. Phys. Chem. C, 118, 24335 (2014).
- 9. J. A. Gilbert et al., J. Electrochem. Soc., 164, A6054 (2017).
- 10. D. R. Gallus et al., *Electrochim. Acta*, **134**, 393 (2014).
- 11. I. Buchberger et al., J. Electrochem. Soc., 162, A2737 (2015).
- 12. X. Liao et al., J. Power Sources, 286, 551 (2015).
- 13. C. Delacourt et al., J. Electrochem. Soc., 160, A1099 (2013). 14. M. Ochida et al., J. Electrochem. Soc., 159, A961 (2012).
- 15. D. R. Vissers et al., ACS Appl. Mater. Interfaces, 8, 14244 (2016).
- 16. K. Leung, Chem. Mater., 29, 2550 (2017).
- 17. R. Jung et al., J. Electrochem. Soc., 166, A378 (2019).
- 18. S. Solchenbach, G. Hong, A. T. S. Freiberg, R. Jung, and H. A. Gasteiger, J. Electrochem. Soc., 165, A3304 (2018).
- 19. O. C. Harris and M. H. Tang, J. Phys. Chem. C, 122, 20632 (2018).
- 20. J. Newman and K. Thomas-Alyea, Electrochemical Systems, 3rd ed., Wiley, New York, (2004).
- 21. M. J. Frisch et al., Gaussian Inc., Wallingford, (2009).
- 22. C. Adamo and V. Barone, J. Chem. Phys., 110, 6158 (1999).
- 23. T. V Russo, R. L. Martin, and P. J. Hay, J. Phys. Chem., 99, 17085 (1995).
- 24. A. V Marenich, C. J. Cramer, and D. G. Truhlar, J. Phys. Chem. B, 113, 6378 (2009).
- 25. A. J. Bard and L. R. Faulkner, Electrochemical Methods Fundamentals and Applications, 2nd ed., Wiley, New York, (2001).
 26. S. Komaba, N. Kumagai, and Y. Kataoka, *Electrochim. Acta*, 47, 1229 (2002).
- 27. A. Jarry et al., J. Am. Chem. Soc., 137, 3533 (2015).
- 28. A. B. P. Lever, *Inorg. Chem.*, 29, 1271 (1990).
- 29. S. Lu, V. V Strelets, M. F. Ryan, W. J. Pietro, and A. B. P. Lever, *Inorg. Chem.*, 35, 1013 (1996).
- 30. V. Balzani, A. Juris, M. Venturi, S. Campagna, and S. Serroni, Chem. Rev., 96, 759 (1996).
- 31. Y. X. Lin et al., J. Power Sources, 309, 221 (2016).
- 32. O. C. Harris, Y. Lin, Y. Qi, K. Leung, and M. H. Tang, J. Electrochem. Soc., 167, 013502 (2020).